

Journal of
Mechanics of
Materials and Structures

**ENERGY-MINIMIZING INCLUSION IN AN ELASTIC PLATE UNDER
REMOTE SHEAR**

Shmuel Vigdergauz

Volume 3, N° 1

January 2008



mathematical sciences publishers

ENERGY-MINIMIZING INCLUSION IN AN ELASTIC PLATE UNDER REMOTE SHEAR

SHMUEL VIGDERGAUZ

A single foreign inclusion perfectly embedded in an elastic plate is considered as a bimaterial setup for finding the interface shape that minimizes the energy increment in a homogeneous shear stress field given at infinity. While simple in concept, this optimization problem is very hard computationally. For tractability, we limit our focus to a narrowed set of curves which can be conformally mapped onto a circle by an analytic function with only one nonzero Laurent term. The resultant one-parameter shape optimization problem with an integral objective functional is then accurately solved using an enhanced complex variable approach. This scheme, though seemingly restrictive, provides good qualitative insight into the optimal solution and bridges the gap between the limiting cases of the energy-minimal hole and the rigid inclusion solved previously.

1. Introduction

Elastostatic analysis and optimization of fiber-reinforced composites is of current interest in various fields of structural engineering, from the traditional mechanical industry [Ibrahim et al. 1991; Bull 1996] to modern nanotechnology [Ovid'ko and Sheinerman 2005] and phononics [Gazonas et al. 2006]. The fibers' shape is of much less practical importance than their volume fraction, though they do significantly influence the overall mechanical behavior. This results in an optimization problem: to maximize structural rigidity of a matrix, determine the shape of a fixed volume of fibers that minimizes the strain energy increment induced in a given homogeneous stress state.

As in other branches of continuum mechanics, the stress-strain analysis of bimaterial structures has advanced much further than the optimization of their mechanical properties. This is true even for the simplest linear two-dimensional case considered here. Closed-form optima such as the equistress inclusion shapes [Vigdergauz 1989] are extremely rare, whereas numerical schemes require a computationally difficult repetitive solution of the fourth-order elasticity equations in the phases domains with a successively modified mutual boundary. The resulting chain of direct boundary value problems becomes especially challenging in a multiconnected domain when a reinforcing phase is arranged into a set of interacting inclusions. This manifests itself in unstable, inaccurate, and too time-consuming computations. It should be pointed out that the difficulties emerge precisely from the computational repetitiveness of the optimization process even though, for any *given* inclusion shape, the stresses and strains can be effectively determined by a wide variety of methods.

Clearly, the optimization is simplified by neglecting fiber interaction. Motivated by this, we consider here the relatively simple but nontrivial case of a single inclusion perfectly embedded into an unbounded

Keywords: plane elasticity problem, Kolosov–Muskhelishvili potentials, shape optimization, effective energy, extremal elastic structures, genetic algorithm.

and homogeneous medium that maintains at infinity the elastic fields $\sigma_{xx}^\infty = P$, $\sigma_{yy}^\infty = Q$, $\sigma_{xy}^\infty = 0$. The exact formulation reads:

Given the single inclusion matrix topology, uniform static far-field loading, and the elastic properties of both materials, find from among all admissible continuous curves the interface shape that minimizes the ratio of the induced energy increment δW to the inclusion area.

For definiteness, the applied stresses are usually taken as either bulk load, that is, $P = Q$, or pure shear, that is, $P = -Q$. The first case is much simpler than the second. For the bulk load, one may use the principle of equistress boundary [Cherepanov 1974; Vigdergauz 1989] to reduce the matrix-inclusion interaction along the optimal interface to a uniform normal pressure. The energy-minimizing inclusion is then a circle regardless of elastic moduli of the phases. This principle does not apply to anisotropy induced by shear loading. Instead, one may resort to a complex variable technique to perform semianalytical optimization in the limiting cases of a hole [Vigdergauz and Cherkayev 1986; Vigdergauz 2006] and infinitely-rigid inclusion [Vigdergauz 2007]. Numerically, this approach leads to a resolving system of linear algebraic equations with closed form coefficients obtained through the following steps:

- (i) The biharmonic Airy function in the matrix region is equivalently replaced with a pair of complex-valued holomorphic functions, the Kolosov–Muskhelishvili potentials [Muskhelishvili 1975].
- (ii) This region is conformally mapped onto the exterior of a circle with the Laurent terms of the mapping function serving as the optimizing design variables. In practice, they are necessarily truncated after a small number of nonzero terms.
- (iii) As a result, the KM potentials are transformed into new holomorphic functions which are then expanded outside the circle into orthogonal Laurent series.
- (iv) Finally, satisfying the boundary conditions (zero tractions for a hole, or zero displacements for a rigid inclusion) gives the required system in the KM expansion coefficients. Due to the basis orthogonality, a finite term mapping gives *exactly* a finite size system, with the closed form entries linearly expressed through the Laurent mapping terms and integers [Vigdergauz and Cherkayev 1986; Vigdergauz 2006; 2007].

Both resulting shapes look like a slightly rounded square. For the optimal hole, the square is aligned with the main stresses P , Q , whereas, for the optimal rigid inclusion, it is rotated from them by 45 degrees.

An *elastic* inclusion involves a second pair of the KM potentials, those *inside* the inclusion. Both pairs are linked through the perfect contact conditions along the interface and hence are to be treated together. It is well known, however, that no curve can have its inner and outer domains mapped simultaneously. For this reason, the third step above becomes impossible and hence the whole scheme cannot be applied, at least straightforwardly.

Shenfeld et al. [2005] proposed an alternative approach for use with a direct FEM solver with adaptive meshing. They performed a reanalysis inside using a specially tailored conjugate gradient method. This combination appears to perform well only for a hole or for a rather rigid inclusion; otherwise, the process fails to converge. The genetic algorithm [Vigdergauz 2001], though highly effective for a hole, suffers otherwise from the same drawback. Both schemes define the shape through a large number of equally spaced nodal points, which are then taken as design variables.

This suggests reconsidering the more economical representation achieved by the above mapping scheme and adapting its third step for elastic inclusions. The untransformed potentials should be directly expanded in their *physical domains* in a nonorthogonal basis, and the conformal mapping should serve only to parameterize the shape. This modification alters the prior numerical performance in two ways, both stemming from the allowed nonorthogonality. The resolving system remains *infinite* for a finite-term mapping, but the closed forms for its coefficients now involve *infinite* sums. All other advantages of the complex-variable approach remain. It permits developing a stable and sensitive optimization scheme that is in line with the approach used for the limiting cases of a hole and a rigid inclusion. The corresponding values of the energy minimum are used as a benchmark to control the computations. Importantly, both cases converge rapidly after increasing the number of mapping terms: even the one term approximation error is less than 0.36% (see Table 1 as extracted from [Cherkaev et al. 1998] and [Vigdergauz 2006]). The error should decrease further for elastic inclusions having less contrast shear moduli. In other words, the simplest possible configuration provides acceptable accuracy at rather low computational cost. For these reason, we concentrate here on this one term scheme and obtain detailed optimization results for all admissible values of the elastic parameters.

The paper is structured as follows. Section 2 formulates the elastostatic boundary value problem for the matrix-inclusion layout. On this basis, the scheme for analytically assessing the energy increment dependence of the inclusion shape is developed in Section 3 and Section 4 with some details moved to Appendix A and Appendix B. Section 5 develops the optimization's computational framework. In Section 6, the proposed scheme is validated by comparing the simulation results with the limiting cases' exact solutions. We present and discuss the numerical results in Section 7 and summarize the main findings in Section 8.

2. Complex variable formulation of plane elasticity

2.1. The forward problem in a bimaterial structure. Figure 1 shows the two phase arrangement in an infinite plate S with an interface L enclosing the origin of the Cartesian system (x, y) . Here and throughout, we use the indexes $j = 1$ and $j = 2$ to identify the inclusion the matrix, respectively. The curve L divides the plate in two parts S_1 and $S_2 = S - S_1$. To each we associate isotropic and homogeneous phases with planar shear moduli μ_j and Poisson ratios ν_j .

To begin, remotely load the plane by an asymptotically uniform stress tensor σ^∞ with components

$$\sigma_{xx}^\infty = P, \quad \sigma_{yy}^\infty = Q, \quad \sigma_{xy}^\infty = 0. \quad (1)$$

Define $z = x + iy$ to be the complex variable in the plane S . Then the inclusion distorted field $\sigma = \{\sigma_{xx}, \sigma_{yy}, \sigma_{xy}\}$ is linearly expressed at any point $z \in S$ through the first two derivatives of the coupled KM analytical potentials $\varphi_j(z)$ and $\psi_j(z)$, which are defined in the subdomains S_j [Muskhelishvili 1975]. For $z \in S_j$,

$$\begin{aligned} \text{Tr}\{\sigma(z)\} &= \sigma_{xx}(z) + \sigma_{yy}(z) = 4\Re\varphi_j'(z), \\ \text{Dev}\{\sigma(z)\} &= \sigma_{yy}(z) - \sigma_{xx}(z) = 2\Re[\bar{z}\varphi_j''(z) + \psi_j'(z)], \\ \sigma_{xy}(z) &= \Im[\bar{z}\varphi_j''(z) + \psi_j'(z)]. \end{aligned} \quad (2)$$

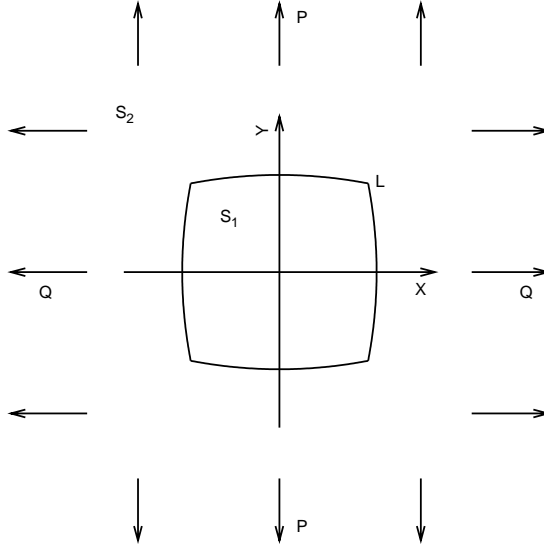


Figure 1. The problem schematic: an infinite plate with a perfectly embedded elastic inclusion under uniform stresses. The cases $P = Q$ and $P = -Q$ correspond to remote bulk and shear. The piecewise smooth hole boundary has a discrete rotational symmetry and may have a finite number of angular points.

Across the interface L , the assumed continuity of the tractions and the displacements links the boundary values of the KM potentials as [Muskhelishvili 1975]

$$\begin{aligned} \overline{\varphi_1(t)} + \bar{t}\varphi_1'(t) + \psi_1(t) &= \overline{\varphi_2(t)} + \bar{t}\varphi_2'(t) + \psi_2(t), \\ \lambda_1 \overline{\varphi_1(t)} - \bar{t}\varphi_1'(t) - \psi_1(t) &= \mu_{12}[\lambda_2 \overline{\varphi_2(t)} - \bar{t}\varphi_2'(t) - \psi_2(t)], \end{aligned} \quad (3)$$

where $\mu_{12} = \mu_1/\mu_2$, $\mu_2 \neq 0$, and $t \in L$. Here

$$\lambda_j = \frac{3 - \nu_j^{(\text{stress})}}{1 + \nu_j^{(\text{stress})}}, \quad \nu_j^{(\text{stress})} \in [0, 1], \quad \text{for plane stress,} \quad (4)$$

$$\lambda_j = 3 - 4\nu_j^{(\text{strain})}, \quad \nu_j^{(\text{strain})} = \frac{\nu_j^{(\text{stress})}}{1 + \nu_j^{(\text{stress})}} \in [0, 0.5], \quad \text{for plane strain.} \quad (5)$$

The unobservable negative values of ν_j are excluded from the numerical simulations (see Section 7). Then both cases $j = 1, 2$ share the interval $1 \leq \lambda_j \leq 3$. The λ_j , together with the shear moduli ratio μ_{12} , serve as unified elastic parameters of the problem.

In the limiting cases of a hole ($\mu_{12} = 0$) or an infinitely rigid inclusion ($\mu_{12} \rightarrow \infty$), the contact relations Equation (3) degenerate to one condition of zero tractions or zero displacements, respectively

[Muskhelishvili 1975]:

$$\begin{aligned}\overline{\varphi_2(t)} + \bar{t}\varphi_2'(t) + \psi_2(t) &= 0, & \text{for a hole,} \\ \lambda_2\overline{\varphi_2(t)} - \bar{t}\varphi_2'(t) - \psi_2(t) &= 0, & \text{for a rigid inclusion.}\end{aligned}$$

For reference, we note that the second goes into the first by formally putting $\lambda_2 = -1$. This is the Dundurs correspondence [Jasiuk 1995]. This fact makes it possible to express the matrix side stresses on L in a form not involving the second potential $\psi_2(t)$ [Vigdergauz 2007], as

$$\begin{aligned}\sigma_{\rho\rho}(t) &= (\lambda_2 + 1)\Re\varphi_2'(t), \\ \sigma_{\theta\theta}(t) &= (3 - \lambda_2)\Re\varphi_2'(t), \\ \sigma_{\rho\theta}(t) &= (\lambda_2 + 1)\Im\varphi_2'(t),\end{aligned}\tag{6}$$

where $t = \rho e^{i\theta} \in L$. The local von Mises equivalent stresses $\sigma_M^2 = (\sigma_{\rho\rho} + \sigma_{\theta\theta})^2 + \sigma_{\rho\theta}^2 - 3\sigma_{\rho\rho}\sigma_{\theta\theta}$ at t can also be combined from Equation (6) in similar fashion, so that

$$\begin{aligned}\sigma_M^2(t) &= D_1(\lambda)(\Re\varphi_2'(t))^2 + D_2(\lambda)(\Im\varphi_2'(t))^2, \\ D_1(\lambda) &= 7 - 6\lambda + 3\lambda^2, \\ D_2(\lambda) &= 3(1 + \lambda)^2.\end{aligned}\tag{7}$$

Of course, at $\lambda_2 = -1$ the above relations transform into the traction-free conditions $\sigma_{\rho\rho}(t) = \sigma_{\rho\theta}(t) = 0$.

Finally, homogeneous loads (1) yield the far field asymptotics

$$\begin{aligned}\varphi_2(z) &= Bz + a_1^{(2)}z^{-1} + O(|z|^{-2}), \\ \psi_2(z) &= \Gamma z + b_1^{(2)}z^{-1} + O(|z|^{-2}), \\ 4B &= \text{Tr}\{\sigma^\infty\} = P + Q, \\ 2\Gamma &= \text{Dev}\{\sigma^\infty\} = Q - P.\end{aligned}\tag{8}$$

At the chosen bimaterial topology, the initial problem of finding the local stresses and strains is equivalent to the homogeneous boundary value problem (3) in the analytic functions $\varphi_j(z)$, $\psi_j(z)$ with a nonzero right hand side given by Equation (8).

The normalized energy increment has the form (see for instance [Jasiuk 1995])

$$\delta W = 2\pi f_1^{-1} \left(2\Gamma a_1^{(2)} + B b_1^{(2)} \right),\tag{9}$$

where f_1 is the inclusion area. Because the stresses are linear in the far loading parameters P and Q , we have

$$a_1^{(2)} = B\alpha_{12} + \Gamma\alpha_{11}, \quad b_1^{(2)} = B\beta_{22} + \Gamma\beta_{21},$$

and hence δW possesses a convenient bilinear form in B , Γ given by

$$\delta W = 2\pi f_1^{-1} \left(2\Gamma^2\alpha_{11} + B\Gamma(2\alpha_{12} + \beta_{21}) + B^2\beta_{22} \right),\tag{10}$$

where α_{12} , β_{22} and α_{11} , β_{21} are computed at the unit trial loadings: for bulk $B = 1$, $\Gamma = 0$, and for pure shear $B = 0$, $\Gamma = 1$, respectively. Though they can be extracted only from the full-scale solution

to Equation (3) and Equation (8), such extraction requires less accuracy than optimizing, say, the local stresses. Next, we will exploit this numerical advantage further by developing a scheme for minimizing δW .

3. Developing the optimization scheme: analytical preliminaries

In our notation, the problem takes the following form:

Given the phase moduli λ_1, λ_2 , and μ_{12} , find the interface shape L that globally minimizes the energy increment of Equation (10) for pure shear ($B = 0, \Gamma = 1$):

$$\delta W(\lambda_1, \lambda_2, \mu_{12}, L) \xrightarrow{\{L\}} \min \equiv \delta W_{min}(\lambda_1, \lambda_2, \mu_{12}). \quad (11)$$

Its numerical treatment requires a nontrivial preliminary analysis which is performed below to the maximum extent.

3.1. Integral criterion for the analyticity of a function. The following development is based on the analyticity of the KM potentials, which can be represented in several equivalent forms. Most relevant here is the set of regular integrals along L as we derived previously in [Vigdergauz 2001]. For convenience, the result is presented here.

Let $\phi_1(z)$ and $\phi_2(z)$ be arbitrary analytic functions of z in S_1 and S_2 with $\phi_2(z)$ linearly growing at infinity, that is, $\phi_2(z) = C_1 z + O(z^{-1})$. Then their boundary values along L obey the following identities in the complementary domains [Gamelin 2001]:

$$J_1(z) \equiv \int_L \frac{\phi_1(t)}{t-z} dt = 0, \quad \text{for all } z \in S_2; \quad J_2(z) \equiv \int_L \frac{\phi_2(t) - C_1 t}{t-z} dt = 0, \quad \text{for all } z \in S_1. \quad (12)$$

By construction, Cauchy-type integrals such as Equation (12) are always analytic [Gamelin 2001]. The Cauchy identity is commonly used for transforming functions into a boundary form with a singularity

$$\begin{aligned} J_1(t_0) &= \frac{1}{2} \phi_1(t_0) + \frac{1}{2\pi i} \int_L \frac{\phi_1(t)}{t-t_0} dt = 0, \\ J_2(t_0) &= \frac{1}{2} (\phi_2(t_0) - C_1 t_0) - \frac{1}{2\pi i} \int_L \frac{\phi_2(t) - C_1 t}{t-t_0} dt = 0, \end{aligned} \quad (13)$$

where $t_0 \in L$, and L is traversed counterclockwise. When L satisfies some minimal smoothness requirements, Equation (12) and Equation (13) are equivalent [Gamelin 2001].

To avoid the boundary singularity, we can use alternatively the analyticity property that implies $J_1(z)$ and $J_2(z)$ remain zero everywhere if they vanish in the circular subdomains $|t/z| < 1$ for $z \in S_2$ and $|z/t| < 1$ for $z \in S_1$. We expand the Cauchy kernel $(t-z)^{-1}$ in the convergent powers series

$$\begin{aligned} \frac{1}{t-z} &= -\frac{1}{z} \sum_{k=0}^{\infty} \frac{t^k}{z^k}, & \left| \frac{t}{z} \right| < 1, & \quad z \in S_2, \\ \frac{1}{t-z} &= \frac{1}{t} \sum_{k=0}^{\infty} \frac{z^k}{t^k}, & \left| \frac{z}{t} \right| < 1, & \quad z \in S_1, \end{aligned} \quad (14)$$

and substitute Equation (14) into Equation (12). Requiring each term vanish yields equivalent sets of resolving identities:

$$\int_L \phi_1(t)t^k dt = 0, \quad \int_L \phi_2(t)t^{-k-1} dt = C_1 \delta_{k,1}, \quad (15)$$

where $k = 0, 1, 2, \dots$ and $\delta_{j,k}$ is the Kronecker delta.

These regular integrals have numerical advantages over their more frequently used singular counterparts of Equation (13).

3.2. Inclusion shape representation.

3.2.1. A circular inclusion. The elastostatic problem of Equation (3) and Equation (8) has a unique solution [Muskhelishvili 1975], at least for any piecewise smooth inclusion shape L . The shape is therefore the only factor influencing the overall numerical difficulty. For instance, a circle $|t| = 1$, $f_1 = \pi$ gives a finite form solution

$$\begin{aligned} \varphi_1(z) &= \frac{\mu_{12}(\lambda_2 + 1)}{2\mu_{12} + \lambda_1 - 1} Bz, & \psi_1(z) &= \frac{\mu_{12}(\lambda_2 + 1)}{1 + \mu_{12}\lambda_2} \Gamma z, \\ \varphi_2(z) &= Bz + \Gamma \alpha_{11} z^{-1}, & \psi_2(z) &= \Gamma z + B\beta_{22} z^{-1} + \Gamma \alpha_{11} z^{-3}, \\ \alpha_{11} &= \frac{\mu_{12} - 1}{1 + \mu_{12}\lambda_2}, & \beta_{22} &= \frac{\mu_{12}(\lambda_2 - 1) - \lambda_1 + 1}{2\mu_{12} + \lambda_1 - 1}, \\ & & \alpha_{21} &= \beta_{12} = 0, \end{aligned}$$

with the energy increment of Equation (10) becoming

$$\delta W_{\text{circle}} = 2B^2 \frac{\mu_{12}(\lambda_2 - 1) - \lambda_1 + 1}{2\mu_{12} + \lambda_1 - 1} + 4\Gamma^2 \frac{\mu_{12} - 1}{1 + \mu_{12}\lambda_2}. \quad (16)$$

It is worth noting that the inclusion potentials $\varphi_1(z)$ and $\psi_1(z)$ are linear in z , and hence, in view of Equation (2), both trial loadings induce a similar constant stress tensor inside a circle $|z| \leq 1$. For bulk loading,

$$\text{Tr}\{\sigma^\infty\} = B = 1, \quad \text{Dev}\{\sigma^\infty\} = \Gamma = 0, \quad (17)$$

$$\implies \text{Tr}\{\sigma(z)\} = 4 \frac{\mu_{12}(\lambda_2 + 1)}{2\mu_{12} + (\lambda_1 - 1)}, \quad \text{Dev}\{\sigma(z)\} = 0, \quad \sigma_{xy}(z) \equiv 0, \quad (18)$$

whereas, for pure shear,

$$\text{Tr}\{\sigma^\infty\} = B = 0, \quad \text{Dev}\{\sigma^\infty\} = \Gamma = 1, \quad (19)$$

$$\implies \text{Tr}\{\sigma(z)\} = 0, \quad \text{Dev}\{\sigma(z)\} = 2 \frac{\mu_{12}(\lambda_2 + 1)}{1 + \mu_{12}\lambda_2}, \quad \sigma_{xy}(z) \equiv 0. \quad (20)$$

The similarity between the remote and inclusion fields is important in the optimization context. Due to the *isotropy* of $\sigma(z)$ in Equation (17), a circle provides the global minimum for δW under *isotropic* bulk loading [Vigdergauz 1989]. In contrast, it remains unknown whether the *full anisotropy* of $\sigma(z)$ in

[Equation \(19\)](#) provides the energy minimum under *anisotropic* pure shear. Numerical evidence relevant to this question is discussed in [Section 7](#).

3.2.2. A general shape. Other shapes can be treated only numerically. Within the complex variable formulation, a typical numerical scheme consists of four consecutive steps:

- (i) transforming the problem [Equation \(3\)](#) with [\(8\)](#) into singular integral equations for the complex-valued density function $\chi(t)$, $t \in L$ along the material's interface. Discussed by [Greengard and Helsing \[1998\]](#), the idea dates back to [Sherman \[1959\]](#);
- (ii) converting the equation into an infinite system of linear algebraic equations in the Fourier amplitudes of $\chi(t)$:

$$\chi(t) = \sum_{k=1}^{\infty} a_k t^k + b_k t^{-k};$$

(iii) solving numerically the truncated system;

- (iv) restoring the finite-term approximation for the potentials by integrating $\chi(t)$ and related quantities over L . Here, the difficulties are transferred to stage (ii) because the system coefficients involve hard-to-compute integrals of rapidly oscillating functions along L .

For stage (ii), [Greengard and Helsing \[1998\]](#) use the fast multipole method, an adaptive quadrature technique, and other advanced procedures to achieve impressive results in computing the stress field for a generally shaped interface. Clearly, the algorithm works much faster for a smooth shape when the time-consuming integration over singularities can be simplified without loss of accuracy to the trapezoidal rule.

In numerical experiments, [Greengard and Helsing \[1998\]](#) parameterize the interface shape using a Fourier series over a unit circle γ :

$$t = \sum_{k=1}^{\infty} g_k \xi^k + h_k \xi^{-k}, \quad (21)$$

where $t \in L$, $\xi = e^{i\eta} \in \gamma$, and $0 \leq \eta \leq 2\pi$. This is exemplified by the *nine-armed* contour:

$$\begin{aligned} t &= 0.36(1 + 0.36 \cos 9\eta)e^{i\eta} = g_1 \xi + g_{10} \xi^{10} + h_8 \xi^{-8}, \\ g_1 &= 0.36, \quad g_{10} = h_8 = 0.18, \end{aligned} \quad (22)$$

where all other g_i and h_i vanish. [Greengard and Helsing \[1998\]](#) calculated numerically the integral-type coefficients of the resolving algebraic system in stage (ii). However, for on-circle parameterizations such as [Equation \(22\)](#), we can obtain the coefficients analytically, using the residue technique [[Gamelin 2001](#)]. This feature could save time in analyzing structures modified repeatedly. However, computations (not reported here) show the optimization process has an instability caused by the simultaneous presence of high positive and negative powers of the polar angle Fourier series such as those in [Equation \(22\)](#).

Matters can be substantially improved by presenting the inclusion shape through the boundary values of an analytic mapping function $\omega(\zeta)$ that behaves asymptotically as $C\zeta + o(1)$ and has only negative powers:

$$t = \omega(\theta) = C\tau + \sum_{k=1}^{\infty} d_k \tau^{-k}. \quad (23)$$

$\omega(\zeta)$ maps conformally the region $\Sigma_2 : |\zeta| \geq 1$ outside the unit circle onto the matrix domain S_2 outside L , with correspondence of the infinity point. Without loss of generality, we suppose that $C = 1$ and the coefficients $\{d_k\}$ are real.

In Equation (21) and (23) we use different notations for the circle points to clarify the following. At first glance, (23) might appear to be a only subset of (21) narrowed by dropping the coefficients g_k for $k > 1$. On the contrary, the complex analysis implies that any closed continuous curve can be written in either of the two forms even though there is no pointwise correspondence between them. Actually, both parameterizations are linked through the identity

$$t = \sum_{k=1}^{\infty} g_k \xi^k + h_k \xi^{-k} = \tau(\xi) + \sum_{k=1}^{\infty} d_k \tau(\xi)^{-k},$$

using the transformation function $\tau = \tau(\xi)$ and requiring $|\tau| = |\xi| = 1$. Unfortunately, such $\tau(\xi)$ is not easy to find, even for only one nonzero coefficient g_k , $k > 1$, as in Equation (22). However this is not our aim here. Instead, we truncate the representation (23) after M terms:

$$\omega(\zeta) = \zeta + \sum_{k=1}^M d_k \zeta^{-k},$$

where $|\zeta| \geq 1$. The expansion coefficients serve as design variables in our previous papers [Vigdergauz 2006; 2007] for the limiting cases of a hole or rigid inclusion. This leads to a novel direct problem solver which is rather fast and stable and can be repetitively used in a successive shape optimization algorithm over the set $C_M(d_1, \dots, d_M)$ of the M -term conformal images of γ . An additional computational option is a p -fold rotational symmetry of the inclusion $\omega(\exp(2i\pi/p)\zeta) = \exp(2i\pi/p)\omega(\zeta)$ in which only the coefficients $\{d_{pk-1}, k = 1, 2, \dots\}$ differ from zero. Here,

$$\omega(\zeta) = \zeta + \sum_{k=1}^M d_{pk-1} \zeta^{-(pk-1)}. \quad (24)$$

In these design variables, the mapping terms possess several useful properties that diminish the problem's computational burden. First, they are subject to successfully narrowing bilateral estimations

$$-\frac{1}{\sqrt{m}} \leq d_m \leq \frac{1}{\sqrt{m}}, \quad m = 1, 2, \dots, \quad (25)$$

that follow from the nonnegativeness of the area f_1 inside γ [Gamelin 2001]

$$f_1 = \pi \left(1 - d_1^2 - 2d_2^2 - \dots - nd_n^2 \right) \geq 0.$$

Second, they are *naturally* ordered, in that the higher the coefficient, the lesser its global impact on the inclusion shape (see Table 1). This argument parallels the fact that the set C_M contains a diverse pool of closed continuous curves even at very small values of M . For instance, the one-term mapping $\omega(\zeta) = \zeta + d_1 \zeta^{-1}$ presents the full family of axes-aligned ellipses with eccentricity $|d_1| \leq 1$, a widely modeled inclusion shape in elasticity studies. Their square symmetric counterparts are exemplified in Figure 2. Finally, as already mentioned, the residue technique routinely gives the integrals of Equation (15) in closed form.

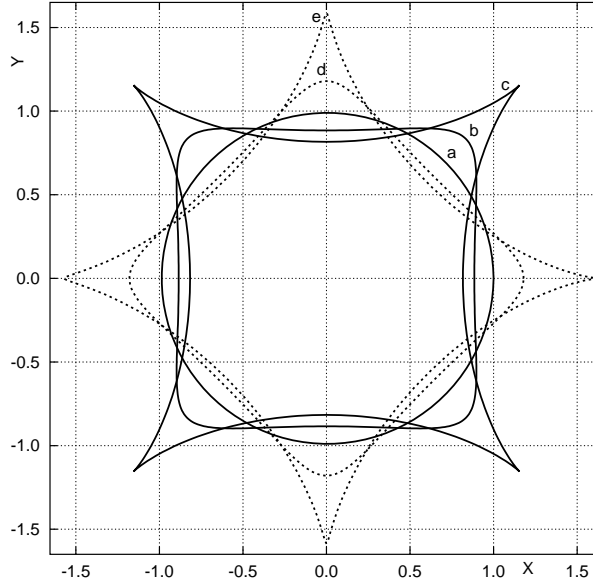


Figure 2. Square symmetric shapes generated from a circle by the one-term mapping $\omega(\zeta) = \zeta + d_3\zeta^{-3}$ for $d_3 = 0$ (a), $d_3 = \mp 0.21$ (b, d, respectively), $d_3 = \mp 1/3$ (c, e). The latter curves present the limiting case of 4-cusped hypocycloids with entrant angles.

In concluding, we note that the first derivative of a single-valued mapping can vanish only inside γ [Gamelin 2001]. For the one-term function $\omega(\zeta) = \zeta + d_m\zeta^{-m}$, that $\omega'(\zeta) = 1 - md_m\zeta^{-m-1} = 0$ only for $|\zeta| < 1$ implies that the inequalities in Equation (25) are sharpened to

$$-\frac{1}{m} \leq d_m \leq \frac{1}{m}.$$

To our knowledge, this has not yet been noticed in the literature.

	Hole [Cherkaev et al. 1998]	Rigid inclusion [Vigdergauz 2006]			
	$\lambda_2 = -1$	$\lambda_2 = 3$	$\lambda_2 = 2$	$\lambda_2 = 1.4$	$\lambda_2 = 1$
N=1	3.6E-03	1.0E-04	4.5E-04	1.5E-03	3.6E-03
N=2	7.7E-04	6.2E-06	5.3E-05	2.6E-04	7.7E-04
N=3	2.5E-04	6.9E-07	1.1E-05	7.1E-05	2.5E-04
N=4	9.6E-05	9.9E-08	2.8E-06	2.0E-05	9.6E-05
N=5	3.1E-05	1.5E-08	6.5E-07	1.7E-06	3.1E-05

Table 1. The limiting cases: the relative error $(\delta W(N)/\delta W(6) - 1)$ of the minimum energy increment versus the number of the first nonzero mapping terms, N . The value $\delta W(6)$ is nearly exact. The outside error columns coincide due to the Dundurs correspondence.

4. The one-potential solving scheme

We are now in a position propose a scheme for solving the forward elastostatic problem. First, we note that the previous section's stage (i) for deriving the singular integral equation is redundant. The contact conditions [Equation \(3\)](#) can be directly transformed into an infinite set of regular integrals along L that involve only the first potentials $\varphi_{1,2}(t)$. This set serves as a pattern for obtaining a resolving system algebraic equations such as those in stage (ii).

Here we use that, in contrast to $\varphi_{1,2}(z)$, the second potentials $\psi_{1,2}(z)$ appear in the boundary conditions of [Equation \(3\)](#), and they are neither conjugated nor differentiated. This makes it possible to separate the potentials and hence to economically find them in sequence rather than in parallel. In doing so, we first exclude $\psi_{1,2}(z)$ from consideration. Solving the algebraic relations of [Equation \(3\)](#) for them, we have

$$(1 - \mu_{12}) \psi_1(t) = (\lambda_1 + \mu_{12}) \overline{\varphi_1(t)} - (1 - \mu_{12}) \bar{t} \varphi_1'(t) - \mu_{12} (1 + \lambda_2) \overline{\varphi_2(t)}, \quad (26)$$

$$(1 - \mu_{12}) \psi_2(t) = (1 + \lambda_2) \varphi_1(\bar{t}) - (1 - \mu_{12}) \bar{t} \varphi_2'(t) - (1 + \lambda_2 \mu_{12}) \varphi_2(\bar{t}). \quad (27)$$

Inserting the right-hand sides of [Equation \(26\)](#) as integrands for the analyticity conditions in [Equation \(15\)](#) and making use of [Equation \(8\)](#), we arrive at an infinite set of identities in $\varphi_{1,2}(z)$. In the second step, we evaluate the resultant integrals involving the boundary values of $\varphi_{1,2}(z)$ and their first derivatives multiplied by powers of t . With [Equation \(8\)](#), we simply expand the sought-for functions in converging series inside and outside L :

$$\varphi_1(z) = \sum_{m=1}^{\infty} a_m^{(1)} z^m, \quad \varphi_2(z) = B + \sum_{m=1}^{\infty} a_m^{(2)} z^{-m}(z). \quad (28)$$

Their substitution results finally in the infinite system of algebraic equations in $a_m^{(1,2)}$, where only the unknown $a_1^{(2)}$ is required for finding the energy increment δW at pure shear when, in conformity with [Equation \(10\)](#),

$$\delta W = 4\pi f_1^1 \Gamma^2 \alpha_{11}. \quad (29)$$

Here again, $\alpha_{11} = a_1^{(2)}$ at $B = 0$ and $\Gamma = 1$.

Some local characteristics of the resultant stress field can be evaluated without the second potential $\psi_{1,2}(z)$. For instance, in view of [Equation \(2\)](#), the trace $\text{Tr}\{\sigma(t)\}$ along the inclusion-matrix interface has a form involving only the potential $\varphi_{1,2}(t)$. However, in contrast to the integral relation of [Equation \(29\)](#) for δW , here the remaining unknowns $a_k^{(1,2)}$ also enter in the resultant expressions through [Equation \(28\)](#). Numerically, this manifests in high frequency oscillations about the true values (the Gibbs phenomenon) as exemplified in [Section 6](#).

In the optional final step, the second potential $\psi_{1,2}(z)$ can be immediately computed through [Equation \(26\)](#), if we are interested in the individual local stresses of [Equation \(2\)](#).

5. The computational framework

In computational practice, the infinite resolving system is truncated to a finite size as

$$\begin{pmatrix} -(\lambda_2 \mu_{12} + 1)A_{11}^{(0)} - (1 - \mu_{12})A_{11}^{(1)} & (\lambda_1 + \mu_{12})A_{12} \\ -\mu_{12}(1 + \lambda_2)A_{21} & (1 + \lambda_2)A_{22}^{(0)} - (1 - \mu_{12})A_{22}^{(1)} \end{pmatrix} X = B, \quad (30)$$

where the A_{ij} are $N \times N$ matrices whose elements are linear in the boundary integrals

$$J_{m,n}^{(1)} = \frac{1}{2\pi i} \int_L t^m \bar{t}^n dt, \quad J_{m,n}^{(2)} = \frac{1}{2\pi i} \int_L t^{m+n} \bar{t} dt, \quad (31)$$

where $m, n = \pm 1, \pm 2, \dots$ and there are no elastic constants involved. The $(2N)$ -element vector of unknowns takes the form

$$X = (a_1^{(2)}, a_2^{(2)}, \dots, a_N^{(2)}, a_1^{(1)}, a_2^{(1)}, \dots, a_N^{(1)}).$$

For pure shear, the right-hand side B has zeroes in all places but the first, which is equal to $(1 - \mu_{12})$. When $\mu_{12} = 1$, the homogeneous system [Equation \(30\)](#) returns all unknowns as zero. Physically, this is because the far-field shear stress is not disturbed by any inclusion shape if both materials have the same shear modulus. Further, when the moduli are almost the same with $\mu_2 = \mu_1 + \varepsilon$, $\|\varepsilon\| \ll 1$, the first order ε -approximation of δW is independent of the inclusion shape, as proven analytically in [Appendix A](#).

In the general case, the system [Equation \(30\)](#) must be treated numerically. Though only the first unknown $a_1^{(2)}$ is required for finding the energy increment, we prefer finding the full vector X for control purposes. We solve the system using the standard LU -decomposition with iterative refinement. This requires $8N^3/3 + 2N^2 + N$ operations which are performed for better accuracy in double-precision arithmetic.

However, in the entire computation, the most time-consuming stage is evaluating the integrals of [Equation \(31\)](#). As already mentioned, this is done analytically by summing the residues at the integrand poles. Deriving the needed expressions involves complicated algebra, especially if the mapping has multiple terms. As a technical simplification, we consider here only a one-term mapping as [Equation \(24\)](#) for the p -fold rotational symmetry: $\omega(\zeta) = \zeta + d_{p-1}\zeta^{-p+1}$. The optimization problem of [Equation \(11\)](#) then becomes

$$\delta W(\lambda_1, \lambda_2, \mu_{12}, d_{p-1}) \xrightarrow{\{d_{p-1}\}} \delta W_{min}(\lambda_1, \lambda_2, \mu_{12}), \quad (32)$$

where

$$f_1 = 1 - (p-1)d_{p-1}^2, \quad -\frac{1}{p-1} \leq d_{p-1} \leq \frac{1}{p-1}. \quad (33)$$

Single-term expressions for the integrals are given in [Appendix B](#). The shape optimization over d_{p-1} in the interval in [Equation \(33\)](#) is then performed by the standard GA scheme with a 32-bit representation of random numbers.

At first glance, the problem [Equation \(32\)](#) with [Equation \(33\)](#) is disappointingly simple compared to the initial formulation in the [Introduction](#). We emphasize again that our choice is justified quantitatively by the accurate one-term results displayed in [Table 1](#) for the limiting cases with the most contrasting shear moduli. Though it does not capture the optimum's fine details, already this approximation leads to nontrivial results not yet reported in the literature.

6. Numerical validation of the optimization scheme

In this section, we assess the performance of the proposed approach by comparing it against the one-term exact solutions. They are known for the limiting cases of the hole and rigid inclusion [[Vigdergauz 2007](#)].

Apparently, the optimal shapes differ from circles only for square symmetry ($p = 4$):

$$\begin{aligned} \delta W_3 &= \frac{\lambda_2}{(\lambda_2 + d_3)(1 - 3d_3^2)}, & d_3^{(min)} &= \frac{\sqrt{\lambda_2^2 + 1} - \lambda_2}{3}, \\ \min_{d_3} \delta W_3 &= \frac{9\lambda_2}{2(2\lambda_2 + \sqrt{\lambda_2^2 + 1})(1 - \lambda_2^2 + \lambda_2\sqrt{\lambda_2^2 + 1})}, \\ \varphi_2(\tau) &= -\frac{\tau^2}{(\lambda_2 + d_3)(1 - d_3\tau^4)}, \quad \text{where } \tau = e^{i\theta} \in \gamma, \end{aligned} \quad (34)$$

and where the negative value of the radical $\sqrt{\lambda_2^2 + 1}$ is taken for the hole with $\lambda_2 = -1$.

We first use these analytical results to choose a compromise value for N in the truncated system of Equation (30), so that a reasonably accurate energy assessment can be obtained at a moderate computational cost. As N increases, Table 2 shows the convergence to the exact value of $\min \delta W_3$. We take $N = 24$ for further computations. This relatively large number is the price paid for using the nonorthogonal expansions of Equation (28).

As could be expected, the local von Mises stresses Equation (7) are computed less accurately than the energy increment because of the oscillations around the exact values (see Figure 3, Figure 4). These oscillations are caused not only by the nonorthogonal expansion basis Equation (28) but also by truncating the resolving infinite system to a finite size. The net effect of the truncation on the oscillations is nicely shown in [Cherkaev et al. 1998], where the transformed KM potentials are orthogonally expanded outside a unit circle. We note that the oscillations are not eliminated completely by increasing N . Only the analytical solution of the infinite system by finite differences [Vigdergauz 2006; 2007] yields in the limiting cases the exact results of the type in Equation (34). Alternatively, the oscillations can be mitigated using filter techniques (see, for example, Laverty and Gazonas [2006]). This subject deserves a separate study.

	Hole $\lambda_2 = -1$		Rigid inclusion			
	δW	E_{rel}	$\lambda_2 = 2$	E_{rel}	$\lambda_2 = 1.4$	E_{rel}
	0.931980515		0.980355859		0.962041131	
$N = 6$	0.916266066	$< 1.7 \times 10^{-2}$	0.980330084	$< 2.6 \times 10^{-5}$	0.960521619	$< 1.6 \times 10^{-3}$
$N = 12$	0.931497017	$< 5.2 \times 10^{-4}$	0.980355816	$< 4.4 \times 10^{-9}$	0.962031339	$< 1.0 \times 10^{-5}$
$N = 18$	0.931913140	$< 7.2 \times 10^{-5}$	0.980355859	$< 1.3 \times 10^{-10}$	0.962040784	$< 3.6 \times 10^{-7}$
$N = 24$	0.931967450	$< 1.4 \times 10^{-5}$	0.980355859	$< 8.9 \times 10^{-11}$	0.962041116	$< 1.6 \times 10^{-8}$
$N = 30$	0.931977621	$< 3.1 \times 10^{-6}$	0.980355859	$< 5.0 \times 10^{-14}$	0.962041131	$< 2.4 \times 10^{-10}$

Table 2. The limiting cases of a hole and a rigid inclusion: the energy minima and their relative deviations from the exact value of Equation (34), as computed for different half-sizes of the resolving system (30) for the one-term square symmetric mapping.

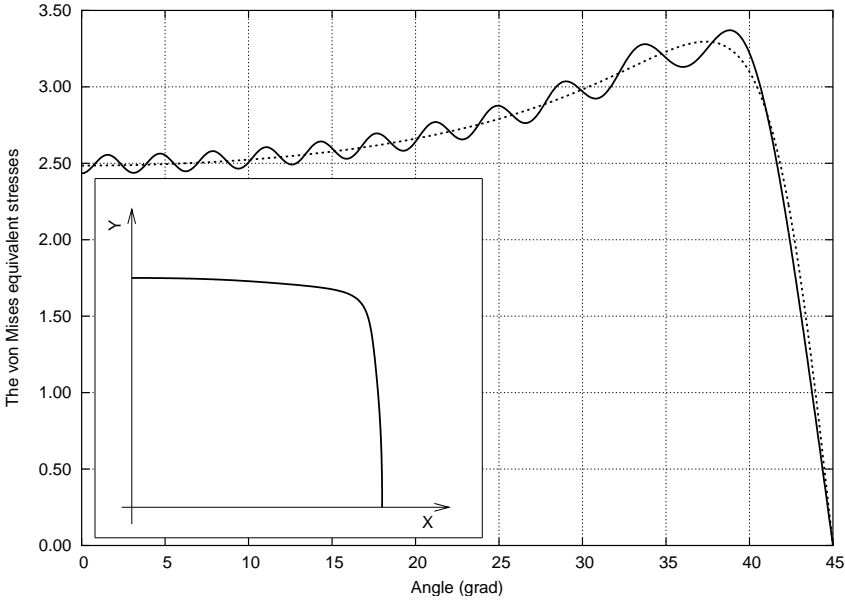


Figure 3. The angular distribution of the von Mises stresses $\sigma_M(t)$ along a quarter of the δW -optimal hole shown in the inset. The computed values stand against the exact result (the dotted line).

7. Numerical results

In the main body of the numerical simulations we detail the dependence of the energy minimum on the elastic parameters of both materials, as seen in the right hand side of Equation (32). To this end, we replace the problem Equation (32) by the three-parameter subproblems ($1 \leq \lambda_{1,2} \leq 3$)

$$\begin{aligned}
 \delta W(\lambda_1, \lambda_2, \mu_{12}, d_{p-1}) &\xrightarrow{\min\{\lambda_1\}, \min\{\lambda_2\}, \min\{d_{p-1}\}} \delta W_m(\mu_{12}), \\
 \delta W(\lambda_1, \lambda_2, \mu_{12}, d_{p-1}) &\xrightarrow{\max\{\lambda_1\}, \max\{\lambda_2\}, \min\{d_{p-1}\}} \delta W_M(\mu_{12}),
 \end{aligned}
 \tag{35}$$

which are solved separately over the discrete set of values $0 < \mu_{12} < 1$ when the inclusion is softer than the matrix, and $0 < \mu_{21} \equiv \mu_{12}^{-1} < 1$ when the inclusion is harder than the matrix. It is of interest that the computed minima of Equation (35) are attained at the *endpoints* of the interval for $\lambda_{1,2}$. This is displayed in Table 3, together with the reference points $\delta W_{m,M}(\lambda_2, \mu_{12})$ for $\mu_{12} = 0, 1, \infty$, which are already known from Equation (34). Recall that $\lambda_{1,2} = 1$ describes an incompressible material.

	$\mu_{12} = 0$	$0 < \mu_{12} < 1$	$\mu_{12} = 1$	$\mu_{12} \geq 1$	$\mu_{12} = \infty$
δW_m	0.931980515...	$\lambda_1 = 3, \lambda_2 = 1$	0.0	$\lambda_1 = 1, \lambda_2 = 1$	0.931980515...
δW_M	0.931980515...	$\lambda_1 = 1, \lambda_2 = 3$	0.0	$\lambda_1 = 3, \lambda_2 = 3$	0.990987403...

Table 3. The parameters $\lambda_{1,2}$ at which the extrema of Equation (35) are attained versus μ_{12} .

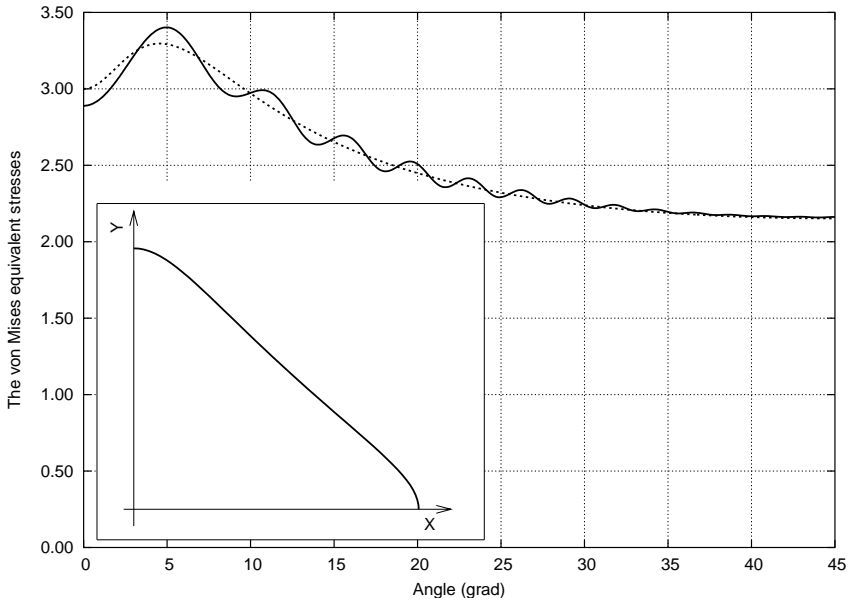


Figure 4. The angular distribution of the matrix-side von Mises stresses $\sigma_M(t)$ along a quarter of the δW -optimal rigid inclusion (shown in the inset). The computed values stand against the exact result (the dotted line).

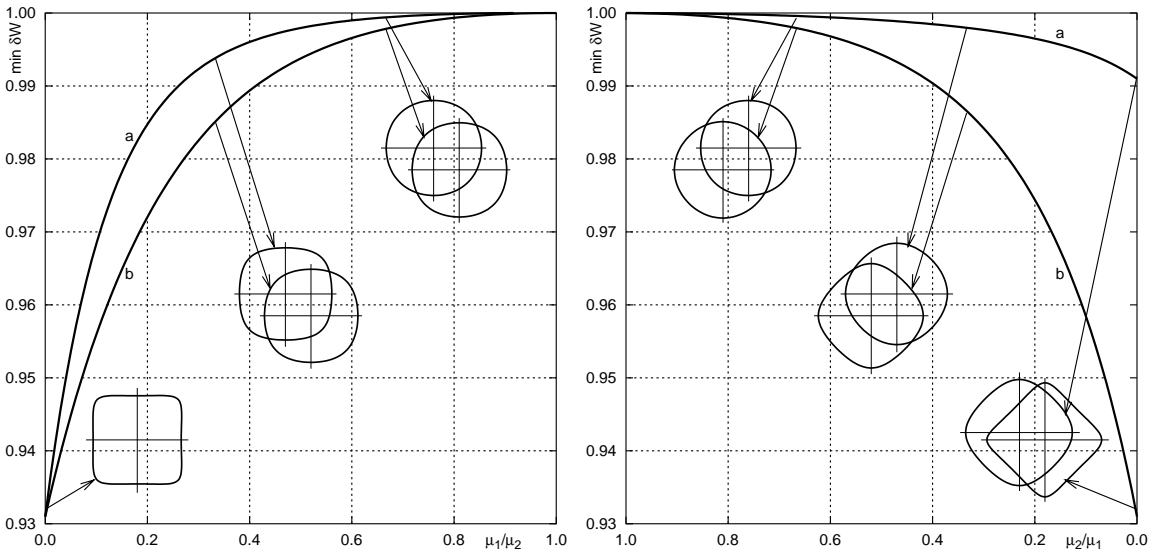


Figure 5. The attainable region of δW_{min} from Equation (36) bounded by $\delta W_M(\mu_{12})(a)$ and $\delta W_m(\mu_{12})(b)$. The evolution of the optimal inclusion shape is also shown by discrete examples.

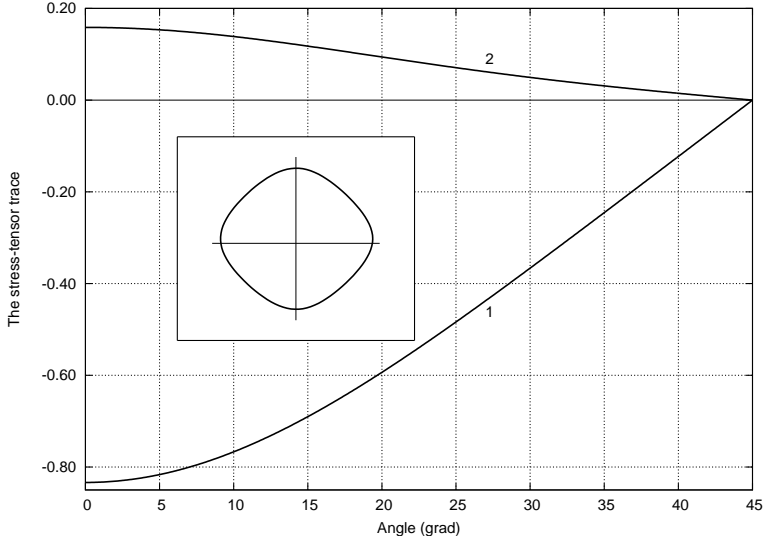


Figure 6. The angular distribution of the matrix-side (1) and inclusion-side (2) stress-tensor trace along a quarter of the δW -optimal inclusion (shown in the inset) at $\mu_{12} = 3$, $\nu_1 = \nu_2 = 0$.

The tabled information is graphed in [Figure 5](#), which depicts the attainable region for $\delta W_{min}(\lambda_1, \lambda_2, \mu_{12})$ in the $(\delta W_{min}, \mu_{12})$ plane:

$$\delta W_m(\mu_{12}) \leq \delta W_{min}(\lambda_1, \lambda_2, \mu_{12}) \leq \delta W_M(\mu_{12}), \quad (36)$$

where $\mu_{12} \in [0, \infty)$ and $\lambda_{1,2} \in [1, 3]$. It would be interesting to know whether each point inside the bounds in [Equation \(36\)](#) at a given μ_{12} corresponds to a pair of Poisson ratios ν_1 and ν_2 . This question is still open, though the affirmative answer seems ‘obvious’.

Finally, [Figure 6](#) shows the distribution of the stress-tensor trace $\text{Tr}\{\sigma(t)\}$ along the optimal inclusion shape. We note that the found local optima are extremely stable against multiple starts of the GA solver.

Three distinctive features seen in the figures support our assumption that the one-term mapping works practically for elastic inclusions.

First, [Figure 5](#) shows that the energy bounds $\delta W_m(\mu_{12})$, $\delta W_M(\mu_{12})$ grow rapidly near the limit points $\mu_{12} = 0, \infty$. In other words, even slightly low contrast materials significantly reduce the energy optimization gain.

Next, the gain is vanishingly small in a reasonably wide vicinity of the point $\mu_{12} = 1$ of the same shear moduli so that very good accuracy is achieved with the first-order approximation of [Equation \(A.6\)](#) in the small parameter $(\mu_{12} - 1)$. We note that the proposed algorithm is here surprisingly stable and accurate in computing small differences between the energy values.

Finally, [Figure 6](#) shows no oscillations in the stress distributions, as opposed to the limiting cases in [Figure 3](#) and [Figure 4](#). This is because the scheme converges faster for low contrast shear moduli. Hence, the local results are sufficiently accurate to conclude that the stress state inside the shear-optimal elastic inclusion has a nonzero trace, in contrast to the circular inclusion as given by [Equation \(19\)](#). However,

we cannot rule out that the trace gradually vanishes for multiterm mappings not considered here. Finally, we note that the optimal shape's large curvature points become less distinctive for low contrast materials (see [Figure 5](#)) and that the shape turns by 45 degrees when passing the point $\mu_{12} = 1$.

8. Concluding remarks

We present a novel numerical scheme for solving the elastic equations for a single-inclusion composite model. This scheme has distinctive features making it highly competitive against other known approaches in assessing the global strain energy and the related quantities.

First, the material interface is presented by a finite-term conformal mapping rather than by nodal points. Regardless of the elastostatic specifics, this expedient enables one to form the initial pool of shapes with a very small number of design variables and hence can be used for optimizing other physical processes in plane two-phase structures.

Next, the KM potentials are computed sequentially rather than in parallel. Finally, the boundary integrals involved are computed analytically (by the residuals) rather than numerically. This stage, though computationally effective, is the most time-consuming part of the algorithm, especially for a multiterm mapping. For this reason, repetitive calculation of the forward problem within an optimization process can be troublesome. Matters can be simplified by using the minimal one-term map which is nevertheless informative enough to provide nontrivial results not previously reported in the literature.

Appendix A: Perturbations of the energy for nearly equal shear moduli

To advance the analytical derivations, we now suppose that $\mu_1 \approx \mu_2$ or, equivalently

$$\mu_{12} = 1 + \varepsilon_\mu + \varepsilon_\mu^2 + \dots, \quad (\text{A.1})$$

where $|\varepsilon| \ll 1$. The continuous K, μ -dependence of the KM potentials allows us expand them also as perturbation series in ε_μ

$$\begin{aligned} \varphi_j(z) &= \varphi_{j,0}(z) + \varphi_{j,1}(z)\varepsilon_\mu + \dots \\ \psi_j(z) &= \psi_{j,0}(z) + \psi_{j,1}(z)\varepsilon_\mu + \dots, \end{aligned} \quad (\text{A.2})$$

where $z \in S_j$, $j = 1, 2$. Substituting [\(A.1\)](#) and [\(A.2\)](#) into [Equation \(3\)](#) and equating the coefficients of equal powers of ε on the left and right hand sides gives:

- (i) At zeroth order, two chained, homogeneous problems in sectionally holomorphic functions $((\lambda_1 + 1)\varphi_1(z), (\lambda_2 + 1)\varphi_2(z))$ and $(\psi_1(z), \psi_2(z))$. For $t \in L$,

$$\begin{aligned} (\lambda_1 + 1)\varphi_{1,0}(t) &= (\lambda_2 + 1)\varphi_{2,0}(t) \\ \psi_{1,0}(t) - \psi_{2,0}(t) &= \overline{\varphi_{2,0}(t)} + \bar{t}\varphi'_{2,0}(t) - \overline{\varphi_{1,0}(t)} - \bar{t}\varphi'_{1,0}(t) \end{aligned} \quad (\text{A.3})$$

with nonzero shear-type asymptotics of [Equation \(8\)](#). As $|z| \rightarrow \infty$,

$$\varphi_{2,0}(z) = O(|z|^{-1}), \quad \psi_{2,0}(z) = \Gamma z + O(|z|^{-1}). \quad (\text{A.4})$$

(ii) At the successive inhomogeneous higher orders, we have, for $t \in L$,

$$\begin{aligned} (\lambda_1 + 1)\varphi_{1,l}(t) - (\lambda_2 + 1)\varphi_{2,l}(t) &= F^{(l)}(t) \equiv \lambda_2\varphi_{2,l-1}(t) - \overline{t\varphi'_{2,l-1}(t)} - \overline{\psi_{2,l-1}(t)} \\ \psi_{1,l}(t) - \psi_{2,l}(t) &= \overline{\varphi_{2,l}(t)} + \bar{t}\varphi'_{2,l}(t) - \overline{\varphi_{1,l}(t)} - \bar{t}\varphi'_{1,l}(t), \end{aligned} \quad (\text{A.5})$$

for $l = 1, 2, \dots$ and with $\varphi_{2,l}(z), \psi_{2,l}(z)$ vanishing at infinity.

In view of (A.4), the unique solution of the homogeneous problem of (A.3) is an identically vanishing $\varphi_{j,0}(z) \equiv 0$, for $z \in S_1 + S_2$ and $j = 1, 2$. Hence

$$\psi_{j,0}(z) = \Gamma z$$

for the same z and j . Substituting (A.4) into (A.5) at $l = 1$ yields the first-order boundary value problem for $\varphi_{1,2}(z)$. For $t \in L$,

$$(\lambda_1 + 1)\varphi_{1,1}(t) - (\lambda_2 + 1)\varphi_{2,1}(t) = -\Gamma\bar{t},$$

which is immediately solved through the Cauchy-type integral

$$(\lambda_j + 1)\varphi_{j,1}(z) = -\frac{\Gamma}{2\pi i} \int_L \frac{\bar{t} dt}{t - z};$$

for $z \in S_j$. This permits finding the first-order approximation for the coefficient $a_1^{(2)}$ entering into the energy increment expression Equation (9) as

$$\begin{aligned} a_{1,1}^{(2)} &= \lim_{z \rightarrow \infty} z\varphi_{2,1}(z) = \lim_{z \rightarrow \infty} \frac{\Gamma}{2\pi i(\lambda_2 + 1)} \oint_L \frac{\bar{t} dt}{1 - t/z} = \frac{\Gamma}{2\pi i(\lambda_2 + 1)} \oint_L \bar{t} dt \\ &= \frac{\Gamma}{2\pi(\lambda_2 + 1)} \oint_L (y dx + x dy) = \frac{\Gamma}{\lambda_2 + 1} f_1. \end{aligned}$$

Taking this expression into Equation (9), we see that the first-order energy increment

$$\delta W_1 = \frac{4\Gamma^2}{(\lambda_2 + 1)} (\mu_{12} - 1) \quad (\text{A.6})$$

depends neither on the inclusion shape L nor the elastic parameter λ_1 . As expected, identity (Equation (A.6)) is consistent with the asymptotic expansion δW_{circle} in Equation (16). The L -dependence of the energy thus first appears at second-order in $(\mu_{12} - 1)$.

Appendix B: Analytical evaluation of the integrals

Our aim here is show the technique for obtaining in closed form the coefficients of Equation (31) for the resolving algebraic system Equation (30). With a finite-term mapping function $t = \omega_n(\tau)$, $\tau \in \gamma$, it can be done using the binomial identities [Abramowitz 1965] to expand the integrands into convergent powers series in τ and integrating them term-by-term over a unit circle γ where the residue theorem [Gamelin 2001] gives

$$\int_{\gamma} \tau^m d\tau = 2\pi i \delta_{m,-1}, \quad (\text{B.1})$$

where $m = 0, \pm 1, \pm 2, \dots$. For concreteness, we consider next the one-term square symmetric mapping $\omega(\tau) = \tau + d_3\tau^{-3}$. Employing the generating polynomials for a nonnegative integer $m = 0, 1, \dots$ [Abramowitz 1965], we use, for $|x| < 1$,

$$(1+x)^m = \sum_{i=0}^m \binom{m}{i} x^i, \quad (1+x)^{-m-1} = \sum_{i=0}^{\infty} \binom{-m}{i} x^i,$$

where

$$\binom{m}{i} = \frac{m!}{i!(m-i)!}, \quad \binom{-m}{i} = (-1)^i \frac{(m+i)!}{m!i!}. \quad (\text{B.2})$$

We arrive at the basic expansions in powers of τ

$$(1+d_3\tau^{\pm 4})^m = \sum_{i=0}^m \binom{m}{i} d_3^i \tau^{\pm 4i}, \quad (1+d_3\tau^{\pm 4})^{-m-1} = \sum_{i=0}^{\infty} \binom{-m}{i} d_3^i \tau^{\pm 4i}. \quad (\text{B.3})$$

With Equation (B.1), substitution of (B.2)–(B.3) into Equation (31) yields separately for positive and negative indices m, n

$$\begin{aligned} J_{-m,-n}^{(1)} &= \int_L \frac{dt}{\bar{t}^{4n-3} t^{4m-2}} = \int_L \frac{\tau^{4(n-m)} (1-3d_3\tau^{-4}) d\tau}{\tau (1+d_3\tau^4)^{4n-3} (1+d_3\tau^{-4})^{4m-2}} \\ &= 2\pi i (S_0 - 3d_3 S_1), \\ S_p &= \sum_{\substack{i=0, \dots, \infty \\ j=0, \dots, \infty \\ \text{s.t. } n-m+j-i=p}} \binom{-(4m-3)}{i} \binom{-(4n-4)}{j} d_3^{i+j}, \quad \text{where } p = 0, 1. \end{aligned} \quad (\text{B.4})$$

Also,

$$J_{-m,-n}^{(2)} = \int_L \frac{\bar{t} dt}{t^{4(m+n-1)}} = \int_L \frac{(1+d_3\tau^4)(1-3d_3\tau^{-4}) d\tau}{\tau^{4(m+n-1)+1} (1+d_3\tau^{-4})} = 2\pi i d_3 \delta_{m+n,2}.$$

The remaining integrals are written similarly

$$\begin{aligned} J_{m,-n}^{(1)} &= \int_L \frac{t^{4m-2} dt}{\bar{t}^{4n-3}} = 2\pi i (T_0 - 3d_3 T_1), \\ T_p &= \sum_{\substack{i=0, \dots, 4m-2 \\ j=0, \dots, \infty \\ \text{s.t. } m+n-i+j=p+1}} \binom{4m-2}{i} \binom{-(4n-4)}{j} d_3^{i+j}, \quad \text{where } p = 0, 1, 2, \end{aligned}$$

and

$$J_{m,n}^{(1)} = \int_L \bar{t}^{4n-1} t^{4m-2} dt = 2\pi i (V_0 - 3d_3 V_1),$$

$$U_p = \sum_{\substack{i=0,\dots,4m-2 \\ j=0,\dots,4n-1 \\ \text{s.t. } m-n-i+j=p}} \binom{4m-2}{i} \binom{4n-1}{j} d_3^{i+j}, \quad \text{where } p = 0, 1, 2.$$

Finally,

$$J_{m,n}^{(2)} = \int_L t^{4(m+n+1)} \bar{t} dt = 2\pi i ((1 - 3d_3^2) W_0 + d_3 (W_{-1} - 3W_1)),$$

$$W_p = \sum_{\substack{i=0,\dots,4m-2 \\ j=0,\dots,4n-2 \\ \text{s.t. } m+n-i-j=p+1}} \binom{4m-2}{i} \binom{4n-2}{j} d_3^{i+j}, \quad \text{where } p = 0, \pm 1. \quad (\text{B.5})$$

Though seemingly cumbersome, identities (B.4)–(B.5) are easily programmed. The infinite sums involved are truncated to their first 16 terms because after that the remainder appears to be below the machine precision (16 bits). To avoid the rounding errors that can occur by using large integers, we employ double precision arithmetic and alternate multiplication with division to compute the binomial coefficients and d_3 powers.

References

- [Abramowitz 1965] M. Abramowitz, *Handbook of mathematical functions, with formulas, graphs, and mathematical tables*, edited by M. Abramowitz and I. A. Stegun, Dover, New York, 1965.
- [Bull 1996] J. W. Bull (editor), *Numerical analysis and modelling of composite materials*, edited by J. W. Bull, Blackie Academic & Professional, London, U.K., 1996.
- [Cherepanov 1974] G. P. Cherepanov, “Inverse problems of the plane theory of elasticity”, *J. Appl. Math. Mech.* **38**:6 (1974), 915–931.
- [Cherkaev et al. 1998] A. V. Cherkaev, Y. Grabovsky, A. B. Movchan, and S. K. Serkov, “The cavity of the optimal shape under shear stresses”, *Int. J. Solids Struct.* **35**:33 (1998), 4391–4410.
- [Gamelin 2001] T. W. Gamelin, *Complex analysis*, UTM series, Springer, New York, 2001.
- [Gazonas et al. 2006] G. A. Gazonas, D. S. Weile, R. Wildman, and A. Mohan, “Genetic algorithm optimization of phononic bandgap structures”, *Int. J. Solids Struct.* **43**:18-19 (2006), 5851–5866.
- [Greengard and Helsing 1998] L. Greengard and J. Helsing, “On the numerical evaluation of elastostatic fields in locally isotropic two-dimensional composites”, *J. Mech. Phys. Solids* **46**:8 (1998), 1441–1462.
- [Ibrahim et al. 1991] I. A. Ibrahim, F. A. Mohamed, and E. J. Lavernia, “Particulate reinforced metal matrix composites - a review”, *J. Mater. Sci.* **26**:5 (1991), 1137–1156.
- [Jasiuk 1995] I. Jasiuk, “Cavities vis-a-vis rigid inclusions: elastic moduli of materials with polygonal inclusions”, *Int. J. Solids Struct.* **32**:3/4 (1995), 407–422.
- [Lavery and Gazonas 2006] R. R. Lavery and G. A. Gazonas, “An improvement to the Fourier series method for inversion of Laplace transforms applied to elastic and viscoelastic waves”, *Int. J. Comput. Meth.* **3**:1 (2006), 57–69.
- [Muskhelishvili 1975] N. I. Muskhelishvili, *Some basic problems of the mathematical theory of elasticity: fundamental equations, plane theory of elasticity, torsion and bending*, 4th ed., Noordhoff, Leiden, the Netherlands, 1975.

- [Ovid'ko and Sheinerman 2005] I. A. Ovid'ko and A. G. Sheinerman, "Elastic fields of inclusions in nanocomposite solids", *Rev. Adv. Mater. Sci.* **9**:1 (2005), 17–33.
- [Shenfeld et al. 2005] V. Shenfeld, D. Givoli, and S. Vigdergauz, "Optimal shape of a grain or a fibre cross-section in a two-phase composite", *Commun. Numer. Meth. Eng.* **21**:2 (2005), 49–60.
- [Sherman 1959] D. I. Sherman, "On the problem of plane strain in non-homogeneous media", pp. 3–20 in *Non-homogeneity in elasticity and plasticity*, edited by W. Olszak, Pergamon Press, New York, 1959.
- [Vigdergauz 1989] S. B. Vigdergauz, "Piecewise-homogeneous plates of extremal stiffness", *J. Appl. Math. Mech.* **53**:1 (1989), 76–80.
- [Vigdergauz 2001] S. Vigdergauz, "Genetic algorithm perspective to identify energy optimizing inclusions in an elastic plate", *Int. J. Solids Struct.* **38**:38-39 (2001), 6851–6867.
- [Vigdergauz 2006] S. Vigdergauz, "The stress-minimizing hole in an elastic plate under remote shear", *J. Mech. Mater. Struct.* **1**:2 (2006), 387–406.
- [Vigdergauz 2007] S. Vigdergauz, "Shape optimization of a rigid inclusion in a shear-loaded elastic plane", *Journal of Mechanics of Materials and Structures = J. Mech. Mater. Struct* **2**:2 (2007), 275–292.
- [Vigdergauz and Cherkayev 1986] S. B. Vigdergauz and A. V. Cherkayev, "A hole in a plate, optimal for its biaxial extension-compression", *J. Appl. Math. Mech.* **50**:3 (1986), 401–404.

Received 10 Mar 2007. Accepted 7 May 2007.

SHMUEL VIGDERGAUZ: smuel@iec.co.il

Research and Development Division, The Israel Electric Corporation Ltd., P.O. Box 10, Haifa 31000, Israel